**Lung inflammation is associated with lipid deposition**

Daria M Potashnikova*, Anna V Tvorogova, Aleena A Saidova, Tatiana N Sotnikova, Eugene A Arifulin, Tatiana V Lipina, Olesya M Shirokova, Eugene S Melnikov, Tatiana A Rodina, Anna A Valyaeva, Anastasia A Zharikova, George O Zayratyants, Oleg V Zayratyants, Eugene V Sheval, Elena J Vasilieva*

**Author affiliations**

**City Clinical Hospital Named After I.V. Davydovsky, Moscow Department of Healthcare, Moscow, Russia**

Daria M Potashnikova, Anna V Tvorogova, Aleena A Saidova, Tatiana N Sotnikova, Eugene S Melnikov, Tatiana A Rodina, Elena J Vasilieva.

**A.I. Yevdokimov Moscow State University of Medicine and Dentistry of the Ministry of Healthcare of the Russian Federation, Moscow, Russia**

Daria M Potashnikova, Oleg V Zayratyants, Elena J Vasilieva.

**Department of Cell Biology and Histology, School of Biology, Lomonosov Moscow State University, Moscow, Russia**

Daria M Potashnikova, Aleena A Saidova, Tatiana V Lipina, Eugene V Sheval

**Belozersky Institute of Physico-Chemical Biology, Lomonosov Moscow State University, Moscow, Russia**

Anna V Tvorogova, Eugene A Arifulin, Anna A Valyaeva, Anastasia A Zharikova, Eugene V Sheval

**Central Scientific Research Laboratory, Institute of Fundamental Medicine, Privolzhsky Research Medical University, Nizhny Novgorod, Russia**

Olesya M Shirokova

**Department of Bioengineering and Bioinformatics, Lomonosov Moscow State University, Moscow, Russia**

Anna A Valyaeva, Anastasia A Zharikova, Eugene V Sheval

**City Clinical Hospital Named After S.S. Yudin, Moscow Department of Healthcare, Moscow, Russia**

George O Zayratyants

**Corresponding authors:**

E.J. Vasilieva

Vasilieva.helena@gmail.com

D.M. Potashnikova

dpotashnikova@gmail.com

**Abstract**

Lung inflammation, pneumonia, is an acute respiratory disease of varying etiology that has recently drawn much attention during the COVID-19 pandemic as lungs are among the main targets for SARS-CoV-2. Multiple other etiological agents are associated with pneumonias. Here, we describe a newly-recognized pathology, namely abnormal lipid depositions in the lungs of patients who died from COVID-19 as well as from non-COVID-19 pneumonias. Our analysis of both semi-thin and Sudan III-stained lung specimens revealed extracellular and intracellular lipid depositions irrespective of the pneumonia etiology. Most notably, lipid depositions were located within vessels adjacent to inflamed regions, where they apparently interfere with the blood flow. Structurally, the lipid droplets in the inflamed lung tissue were homogeneous and lacked outer membranes as assessed by electron microscopy. Morphometric analysis of lipid droplet deposition area allowed us to distinguish the non-pneumonia control lung specimens from the macroscopically intact area of the pneumonia lung and from the inflamed area of the pneumonia lung. Our measurements revealed a gradient of lipid deposition towards the inflamed region. The pattern of lipid distribution proved universal for all pneumonias. Finally, lipid metabolism in the lung tissue was assessed by the fatty acid analysis and by expression of genes involved in lipid turnover. Chromato-mass spectrometry revealed that unsaturated fatty acid content was elevated at inflammation sites compared to that in control non-inflamed lung tissue from the same individual. The expression of genes involved in lipid metabolism was altered in pneumonia, as shown by qPCR and in silico RNA-seq analysis. Thus, pneumonias of various etiologies are associated with specific lipid abnormalities; therefore, lipid metabolism can be considered to be a target for new therapeutic strategies.

**Keywords**

lung pathology; pneumonia; COVID-19; lipid deposition; lipid metabolism

## Statements and Declarations

### Ethical approval

The study was approved by the Moscow City Ethics Committee (protocol № 50/69_13.10.2020) of the Research Institute of the Organization of Health and Healthcare Management and performed according to the Declaration of Helsinki.

### Conflict of interest

The authors declare no competing interests.

### Funding

The work was supported by the ANO "William Harvey" and the Russian Science Foundation (grant 21-74-20134). The funding sources had no role in the design or conduct of the study.

### Data Availability Statement

The R code for the single-cell RNA-seq data analysis is deposited at https://github.com/kirushka/covid19_FAT

### Acknowledgements

The authors are deeply grateful to Prof. Leonid Margolis for his invaluable contribution to this work and the manuscript writing. The authors thank Prof. A.V. Shpektor and Dr. V.N. Manskikh for stimulating discussions and important suggestions, and Dr. Barry Alpher for editing the manuscript.

### Author Contributions

PDM, ShEV conceived and performed the experiments, analyzed the data, provided figures, and wrote the manuscript. TAV and SAA conceived and performed the experiments, analyzed the data, and provided figures. STN, AEA, LTV, ShOM, MES, and RTA performed the experiments and analyzed the data. VAA, ZhAA, and ZGO collected and analyzed the data and provided figures and tables. ZOV and VEJ conceived the experiments, analyzed the data, and wrote the manuscript.

## Introduction

Pneumonias of various etiologies are life-threatening conditions that affect alveoli and distal bronchioles, or interstitial lung tissue. Many morphological [1,2] and physiological [3,4] abnormalities have been reported in inflamed lungs. However, dysregulation of lipid metabolism associated with lung inflammation has been addressed much less, although lipid synthesis in general and lung surfactant specifically have an important role in lung diseases [5]. Recently, different aspects of pneumonia have attracted attention in the context of COVID-19, as the lungs are one of the main target organs of SARS-CoV-2 [6]. However, the lipid metabolism in the context of this infection has not been thoroughly studied.

Here, we addressed this issue by investigating lipids in postmortem lung specimens from individuals who died of pneumonia. The lipids in inflamed lung tissue were deposited as droplets in the cell cytoplasm, in the extracellular space, and within small blood vessels. These lipid depositions were largely restricted to the inflamed area of the lung and were associated with elevated levels of unsaturated fatty acids and generally decreased expression of genes involved in lung lipid metabolism.

To determine whether these lipid abnormalities are characteristic of COVID-19–associated pneumonia, we extended our study to pneumonias of different etiologies. In the lungs of SARS-CoV-2–negative patients who died of pneumonia, we found lipid depositions similar to those in SARS-CoV-2–positive patients. Abnormal lipid deposition may contribute significantly to the development of pathological processes associated with pneumonia.

## Materials and methods

### Autopsies and post-mortem sampling

The study included lung autopsies from 23 patients who died of COVID-19–associated pneumonia (obtained from the Department of Pathology of the City Clinical Hospital named after S.S. Yudin re-profiled for COVID-19 autopsies according to the international and Russian requirements for working with COVID-19), 18 patients who died of pneumonias of other etiologies and 10 lung autopsies were taken from individuals without pneumonia (obtained from the City Clinical Hospital named after I.V. Davydovsky). The autopsy data are provided in Supplementary Table 1. The data on body mass indexes were included to verify whether the changes in tissue organization were related to general obesity.

### Histological specimens

For pneumonia lung autopsies, two 1.0x1.5x0.5-cm tissue specimens were taken from the area with macroscopically distinct inflammation in the inferior lobe of the lung (segments S8 or S9), and another two – from the macroscopically intact area in the superior lobe of the lung (segments S1 or S2). The latter served as an internal control for morphological examination and lipid content analysis. For the non-pneumonia lung autopsies, two specimens were obtained from one site, the macroscopically intact lung tissue (inferior lobe, segments S8 or S9), which served as an external non-inflamed control.

The specimens were fixed in 10% buffered formalin. One was used to make cryosections for Sudan III and Oil Red O/anti-CD31/DAPI staining. The other was dehydrated, cast in paraffin blocks, and used for H&E-staining (hematoxylin and eosin). All dyes for histological staining were provided by Labiko (Moscow, Russia). Paraffin sections 3-4 μm thick were stained with H&E, dehydrated, and mounted in Vitrogel (Biovitrum, Russia). Cryosections 7 μm thick were made using a Leica CM1850 cryotome (Leica, Germany), placed on Superfrost Plus glass slides (Thermo Scientific, US), dried at +60°C, stained with Sudan III by Herxheimer, co-stained with Carazzi hematoxylin

(exposure time 40 sec, three rinses in tap water) mounted in glycerol and imaged using a Leica DM2000 microscope with Leica DFC7000 T camera (Leica, Germany).

**Pathological analysis on semi- and ultrathin sections**

Lung tissue specimens 1x1x1 mm in size were fixed in 2.5% glutaraldehyde (Ted Pella, US) in cacodylate buffer, post-fixed in 1% $OsO_4$, dehydrated in ethanol and propylene oxide (Sigma-Aldrich, US), and embedded in Epon (Fluka, Switzerland). We obtained semi-thin sections (0.5 μm thick) with a Leica ultramicrotome using glass knives and stained them on glass slides using methylene blue/azure II [7] or polychromatic Twort's staining, as described earlier [8] (Supplementary Figure S1A–B). The sections were mounted in Epon resin under a coverslip, and imaged using a Leica DM2000 microscope equipped with a Plan-Neofluar 100/1.3 Oil immersion objective and a Leica DFC7000 T camera.

Ultrathin sections were made using a diamond knife and mounted on slot grids (Ted Pella, US), stained with uranyl acetate and lead nitrate, and examined using a JEM-1400 electron microscope (Jeol, Japan) at an accelerating voltage of 80 kV.

**Morphologic and morphometric analysis of Sudan III-stained specimens**

The specimens selected for the quantitative analysis were from individuals with body mass indexes BMI<30 to exclude the possible effect of obesity on local lipid deposition. One hundred consequential images were assessed for both inflamed and intact Sudan III-stained specimens of lungs with pneumonia and for intact specimens of lungs without pneumonia. Morphological analysis included a blinded examination of 100 images by three independent morphologists. All images were checked for the presence of 1) intracellular lipid droplets (Sudan III–positive droplets in cell cytoplasm), 2) extracellular lipid droplets (Sudan III–positive droplets in the vessel wall or alveolar intercept), and 3) intra-vessel lipid droplets (Sudan III–positive droplets inside blood vessels with/without erythrocytes). The average number of images containing lipid droplets of either kind was expressed as the percentage of images per specimen.

We performed the morphometric analysis of Sudan III–positive areas using Image Pro software (Media Cybernetics, US). Twenty images were randomly selected for each specimen of inflamed and intact pneumonia lung or the intact non-pneumonia lung. For each image, lipid droplets were included in a mask containing pixels by color, adjusted to include all Sudan III–positive structures into the regions of interest (ROIs). The resulting ROIs were assessed as area per image.

**Fluorescence and immunofluorescence specimens**

Cryosections of formalin-fixed lung tissue 7 μm thick were washed in PBS and permeabilized for 1 h with 0.01% Tween 20 (Sigma-Merck, Germany), followed by three washes in PBS. We stained vascular endothelium using a CD31-FITC antibody (clone WM59, BD Biosciences, US) at 1:100 dilution in a humid chamber at +37ºC for 1 h. Oil Red O (Sigma-Merck, Germany) dye was used for staining lipids; sections were stained for 20 min at RT according to the manufacturer's protocol. Nuclei were co-stained with DAPI (Thermo Scientific, US) at a final concentration of 1μg/ml.

Fluorescence imaging was performed in scanning mode using an inverted Zeiss AxioObserver (Zeiss, Germany) microscope operating under Zen 3.1 Blue Edition software with a ×40/Oil objective, standard filter cubes and Hamamatsu ORCA-Flash4.0 V2 camera (Hamamatsu Photonics, Japan). We used ImageJ software (NIH) for image processing.

**Fatty acid profiling by chromato-mass spectrometry**

To determine the fatty acid (FA) profile, we analyzed 10 pneumonia lung specimens. A tissue section was taken from the area with macroscopically distinct inflammation and from the macroscopically intact area of the same lung. Lung tissue was finely cut, aliquoted, weighed, and stored at -40°C prior to analysis. One aliquot was used to determine the moisture content of the sample as the weight loss on lyophilization, another aliquot was used to determine the FA profile.

Thawed specimens were homogenized using glass beads. We extracted lipids using the Folch method [9] and determined the content of 31 FAs using a gas chromatograph mass spectrometer Shimadzu TQ8050 (Shimadzu, Japan). We used chemical ionization with ammonia [10], and chromatographic separation using a DB-23 column (60 m, 0.25 mm, 0.15μm, 122-2361 Agilent, US). FAs were identified on the basis of the retention times of analytes and the fragmentation reactions of quasimolecular ions of carboxylic acid ethyl esters and/or their adducts with ammonia [10]. The total mass of FAs in the specimen and their mass fractions were calculated.

**RNA extraction and reverse transcription**

For total RNA extraction, one lung section 5x5x5 mm in size was finely cut and stored at -20°C in RNAlater (Thermo Scientific, US). We mechanically disrupted the tissue from RNAlater using a MediMachine (BD Biosciences, US) in 700 μL of RLT buffer (Qiagen, Germany) with 1% β-mercaptoethanol (Merck, Germany). The volume of tissue suspension was adjusted to 1.5 mL with nuclease-free water. The homogenate was incubated with 200 μg/mL Proteinase K (Thermo Scientific, US) at +54°C for 50 min and centrifuged for 10 min at 10,000 g. The supernatant was processed according to the RNeasy mini kit protocol (Qiagen, Germany). We eliminated DNA by on-column digestion using RNase-free DNase (Qiagen, Germany). We reverse-transcribed cDNA from total RNA using the ImProm II Kit (Promega, US) with Random primers, according to the manufacturer's instructions.

**Real-time qPCR**

We detected SARS-CoV-2 RNA in total RNA specimens using TaqMan one-step qPCR. We analyzed amplification of two different regions of the SARS-CoV-2 nucleocapsid gene (*N2* and *N3*), simultaneously using primers described earlier [11]. Additionally, the ubiquitin C (*UBC*) gene was used as an internal control in a triplex reaction. The primers and probes are listed in Supplementary Table 2. RNA solution (5 μl per well) was mixed with 5 μl of triplex primer/probe mix and 10 μl of qScript XLT One-Step RT-qPCR Tough Mix (Quantabio, US).

The genes involved in lipid metabolism (*LPL, PLA2G4A, PLA2G2A, COX1, COX2*) were analyzed in cDNA specimens using a Syntol PCR kit (Russia). The TaqMan primers and probes are listed in Supplementary Table 3. The relative quantities of target genes were normalized to the ubiquitin C (*UBC*) reference gene. We analyzed all samples in duplicate using a CFX96 Touch cycler with CFX-Manager software (Bio-Rad, US).

**Meta-analysis of bulk and single-cell RNA-seq datasets**

Published bulk and single-cell RNA-seq data from human COVID-19 lung tissue were re-analyzed to identify lipid metabolism genes with altered expression in pneumonia samples compared to healthy controls. The bulk RNA-seq dataset GSE150316 [12] was obtained from the Gene Expression Omnibus (GEO) database. Single-cell RNA-seq data were downloaded from the SCovid database [13], which accumulated datasets from different studies as lists of differentially expressed genes. We used clusterProfiler (version v3.18.1) [14] to perform functional over-representation analysis and focused on Gene Ontology (GO) terms enriched with differentially expressed genes related to lipid and fatty acid metabolism. Briefly, we used keywords "lipid," "fat," "triglyceride," or "cholesterol" to search the enrichment results for the specific GO categories. For single-cell RNA-seq data, the REVIGO tool [15] was used to remove redundant GO terms.

## Results

### Localization of lipid depositions

First, we examined 12 postmortem COVID-19 lung specimens (specimens COVID-19 ##1–12, Supplementary Table S1). We diagnosed COVID-19 by qPCR of SARS-CoV-2 RNA before/during hospitalization and confirmed it by qPCR of post-mortem lung tissue.

Histological examination revealed loss of alveolar morphology associated with an apparent exudative or proliferative phase of diffuse alveolar damage (Supplementary Figure S2A-E). In congested small vessels, round cavities surrounded by erythrocytes were observed (Fig. 1A-B); a diligent search revealed multiple examples of such cavities, even in a single H&E specimen (Supplementary Figure S3). We hypothesized that they might contain lipid droplets that were removed during routine ethanol dehydration.

To confirm this, we analyzed semi-thin lung sections post-fixed with OsO4 and stained with methylene blue/azure II. Examination of 12 semi-thin specimens of lung tissue clearly revealed large (10–100μm in diameter) OsO4-contrasted lipid droplets inside blood vessels (Fig. 1C-E). These droplets either filled the entire volume of the vessels (Fig. 1C) or were located among erythrocytes (Fig. 1D-E), which corresponded to our findings in the paraffin sections (Fig. 1A-B). We reliably identified droplets in blood vessels in 6 out of 12 patients, which represent rather late stages of the pathological process in the lungs (proliferative stage of pneumonia). Additionally, we found numerous cells inside the blood vessels (neutrophils by morphology) and inside the lung tissue (macrophages by morphology) with small lipid droplets inside the cytoplasm (Fig. 1F).

Electron microscopy (EM) of lipid droplets inside the blood vessels revealed their homogeneous structure (Figure 1G–H). The erythrocytes in contact with these drops changed their shape, indicating significant mechanical toughness and stability of these droplets.

### Quantification of lipid depositions

Next, we assessed lipid droplet deposition using cryosections stained with Sudan III. The frequency of lipid deposition in the specimens of COVID-19–associated pneumonia (specimens COVID-19 ##13–23, Supplementary Table S1) was compared to that in non-COVID-19–associated pneumonias (specimens non-COVID-19 ##1–18, Supplementary Table S1) and non-pneumonia control lung specimens (specimens Ctrl ##1–10, Supplementary Table S1). To spatially analyze lipid deposition during inflammation, we assessed two specimens from different sites in the same lung for each pneumonia case: inflamed tissue from the lower lobe and macroscopically intact tissue from the upper lobe. The non-pneumonia lungs predominantly were Sudan III-negative (Figure 2A) or contained only single Sudan III-positive cells and extracellular droplets (Figure 2B). Intra-vessel lipid droplets were not detected in non-pneumonia specimens. In the inflamed lung, lipid droplets were visible inside cells, in the alveolar and vessel walls, and inside blood vessels. The pattern was similar for COVID-19–associated (Figure 2C–E) and non-COVID-19–associated pneumonias (Supplementary Figure S4A–C). For quantitative analysis, specimens of non-pneumonia lungs (n=3), COVID-19–associated (n=4), and non-COVID-19–associated (n=4) pneumonia were analyzed. The average occurrence of lipid droplets with different localizations was calculated per 100 consequential frames for each specimen and presented as percentage of frames containing intracellular, extracellular, and intravessel droplets (Supplementary Table S4). The number of cells with cytoplasmic lipid droplets was threefold higher in pneumonia specimens (intact and inflamed lung tissue) than in the control non-pneumonia lung tissue, whereas the number of extracellular lipid droplets was fivefold higher in inflamed pneumonia lung tissue than in the control non-pneumonia lung tissue (Figure 2F), the differences were statistically significant (Mann-Whitney test, $p<0.05$). Importantly, intra-vessel lipid droplets were detected in intact and inflamed pneumonia lung tissue, but not in the non-pneumonia control. No significant

differences (Mann-Whitney test, $p>0.05$) in the occurrence of lipid droplets were observed for macroscopically intact vs. inflamed tissues from the same lung or for COVID-19–associated vs. non-COVID-19–associated pneumonia (Figure 2F).

We performed a semi-automated morphometric analysis of the total lipid deposition area (for a representative example of the ROIs, see Supplementary Figure S5). No significant differences in total lipid deposition were found between individual specimens within the groups of non-pneumonia lungs, intact pneumonia lungs, and inflamed pneumonia lungs (1-way ANOVA, Dunns post-test). Therefore, for further analysis, data from individuals were pooled into their respective groups (Figure 2G; Supplementary Table S4). The area of lipid deposition was 63.4±20.5 $\mu m^2$ (mean±SD) per frame in the control non-pneumonia lung tissue, 214.5±170.4 $\mu m^2$ in the intact tissue of non-COVID-19–associated pneumonia, 1,732.3±1,212.0 $\mu m^2$ in the inflamed tissue of non-COVID-19–associated pneumonia, 368.5±67.1 μm2 in the intact tissue of COVID-19–associated pneumonia, and 1,494.4±608.6 $\mu m^2$ in the inflamed tissue of non-COVID-19–associated pneumonia. The differences between all groups were statistically significant (Mann-Whitney test, $p<0.05$) (Figure 2G).

**Fluorescence lipid visualization**

To further facilitate morphometric assessment of lipid distribution in the lung tissue, we developed a protocol of triple fluorescence staining of lung cryosections: lipids were stained with Oil Red O that was combined with the intracellular anti-CD31 and DAPI staining (see Materials and Methods for details). Using the triple staining, we confirmed the localization of lipid droplets inside cells, in the alveolar and vessel walls, and inside blood vessels (Figure 3A–C).

**Fatty acid content in pneumonia**

As morphometric analysis showed elevated levels of lipid deposition in the inflamed *vs* intact regions of lung in pneumonia, we compared the FA content between these sites using chromato-mass spectrometry. The total FA content was not significantly changed in the inflamed tissue compared with the intact tissue of the same lung (Supplementary Figure S6A). However, the unsaturated-to-saturated FA ratio (U/S ratio) was significantly increased in the specimens with inflammation compared to intact lung (Supplementary Figure S6B). Also, we found statistically significant differences in the content of nine individual fatty acids in samples from different sites of the same lung (Supplementary Figure S6C).

**GO analysis and RT-qPCR**

To investigate the metabolic processes underlying lipid accumulation in lung tissue, we employed Gene Ontology (GO) analysis of the available RNAseq datasets (nine independent COVID-19 cases and the data on the cumulative dataset). Importantly, the overall trend for gene downregulation was observed, despite the inter-specimen variability (Supplementary Figure S7A).

At single-cell level, the tendency was confirmed: the downregulated genes prevailed in lung tissue, most notably in fibroblasts, macrophages, and T cells (Supplementary Table S5). Among the downregulated genes in macrophages and endothelial cells, we found ones involved in free fatty acid / cholesterol uptake, storage, and metabolism.

The selected array of genes tested by RT-qPCR included lipases (*LPL, PLA2G4A, PLA2G2A*), which are involved in FA remodeling, and cyclooxigenases (*COX1, COX2*), which drive prostaglandin synthesis and prompt FA transition to inflammation mediators. *PLA2G4A* was downregulated in pneumonias compared to non-pneumonia lungs (Supplementary Figure S7B); *COX1* was downregulated in non-COVID-19–associated pneumonias (Supplementary

Figure S7C) compared to normal lungs and COVID-19–associated pneumonias, whereas *PLA2G2A*, *COX2*, and *LPL* were not differentially expressed.

**Discussion**

Pathological alterations in pneumonias have been thoroughly studied for over a century, and a number of them have been described [16–18]. The recent COVID-19 pandemic significantly increased pneumonia incidence and triggered a new wave of publications on this disease [19,20]. Nevertheless, among the multiple pathologic processes associated with pneumonia, lipid metabolism remains the least studied. Here, we analyzed the post-mortem cases with diagnosed COVID-19–associated pneumonia and non-COVID-19–associated pneumonia to describe the alterations in lipid deposition in the inflamed lung. Specimens of non-pneumonia lungs served as controls.

Lipid depositions were first described morphologically in tuberculosis-associated pneumonia for sites adjacent to the caseous necrosis area in the beginning of the 20th century [21] and were mentioned later in papers describing abnormal lung morphology [22–25]. The scarcity of morphological studies of lipids is partly due to the fact that routine paraffin sections are unsuitable for revealing lipid-rich structures. We addressed this issue using cryosections stained with lipophilic dye and semi-thin sections with $OsO_4$ post-fixation, which stabilizes the lipids [26]. In several recent studies, the authors also found lipid depositions in COVID-19–associated pneumonias [24,25] with alternative techniques, but related this to systemic factors due to patients' obesity [23]. In contrast, we found that such abnormalities are local, are not associated with obesity, and are not restricted to COVID-19–associated pneumonia, but rather are characteristic of lung inflammation in general.

Specifically, in inflamed lung, we identified small lipid droplets localized within cell cytoplasm and large homogeneous intra-vessel lipid droplets, not surrounded by membranes. The latter droplets would apparently block the blood flow and affect gas exchange, one of the key aspects of various pneumonias [20, 27], thus significantly contributing to disease progression.

We observed a gradient of lipid deposition from the inflamed to the unimpaired lung regions. This gradient may be caused by factors spreading outside the inflamed region. Alternatively, lipid metabolism abnormalities may constitute an early event in lung inflammation, and tissue in the upper lung segments, while still macroscopically intact, is presenting the first pneumonia-caused morphological changes. Regardless of the mechanism of this phenomenon, chromato-mass spectrometry revealed a significant shift towards unsaturated FAs in the inflamed lung areas compared to the intact parts of the same lung, confirming that lipid abnormalities are local. These data are in agreement with the lipid level changes in bronchoalveolar lavage fluids associated with ARDS and pneumonia, where a decrease in saturated C16:0 and an increase in unsaturated C18:1 and C18:2 have been reported [28,29]. Lipid deposition may be caused by inflammation-driven shifts in the expression of genes involved in lipid synthesis and turnover [30,31]. In addition, lipid accumulation may result from tissue decomposition in the inflamed areas combined with macrophages' inability to eliminate accumulated lipids [32,33].

In conclusion, our data provide new insights into pneumonia pathogenesis and its association with lipid metabolism and inflammation. Our results indicate that lipid metabolism can be considered a target for therapeutic interventional strategy in pneumonia.

**References**


1. Kradin RL, Digumarthy S (2017) The pathology of pulmonary bacterial infection. Semin Diagn Pathol 34:498–509
2. Pritt BS, Aubry MC (2017) Histopathology of viral infections of the lung. Semin Diagn Pathol 34:510–517
3. Whitsett JA, Alenghat T (2015) Respiratory epithelial cells orchestrate pulmonary innate immunity. Nat Immunol 16:27–35
4. Quinton LJ, Walkey AJ, Mizgerd JP (2018) Integrative Physiology of Pneumonia. Physiol Rev 98:1417–1464
5. Agudelo CW, Samaha G, Garcia-Arcos I (2020) Alveolar lipids in pulmonary disease. A review. Lipids Health Dis 19:122
6. Valyaeva AA, Zharikova AA, Sheval EV (2022) SARS-CoV-2 cellular tropism and direct multiorgan failure in COVID-19 patients: Bioinformatic predictions, experimental observations, and open questions. Cell Biol Int. https://doi.org/10.1002/cbin.11928
7. (2010) Methylene blue/azure II staining solution. Cold Spring Harb Protoc 2010:db.rec12090
8. Manskikh VN, Sheval EV (2020) An adaptation of Twort's method for polychromatic staining of epoxy-embedded semithin sections. Histochem Cell Biol 153:121–127
9. Folch J, Lees M, Sloane Stanley GH (1957) A simple method for the isolation and purification of total lipides from animal tissues. J Biol Chem 226:497–509
10. Schober Y, Wahl HG, Renz H, Nockher WA (2017) Determination of red blood cell fatty acid profiles: Rapid and high-confident analysis by chemical ionization-gas chromatography-tandem mass spectrometry. J Chromatogr B Analyt Technol Biomed Life Sci 1040:1–7
11. Komissarov A, Molodtsov I, Ivanova O, et al (2021) High SARS-CoV-2 load in the nasopharynx of patients with a mild form of COVID-19 is associated with clinical deterioration regardless of the hydroxychloroquine administration. PLoS One 16:e0246396
12. Desai N, Neyaz A, Szabolcs A, et al (2020) Temporal and spatial heterogeneity of host response to SARS-CoV-2 pulmonary infection. Nat Commun 11:6319
13. Qi C, Wang C, Zhao L, et al (2022) SCovid: single-cell atlases for exposing molecular characteristics of COVID-19 across 10 human tissues. Nucleic Acids Res 50:D867–D874
14. Wu T, Hu E, Xu S, et al (2021) clusterProfiler 4.0: A universal enrichment tool for interpreting omics data. Innovation (Camb). 2021; 2 (3): 100141
15. Supek F, Bošnjak M, Škunca N, Šmuc T (2011) REVIGO summarizes and visualizes long lists of gene ontology terms. PLoS One 6:e21800
16. Gill JR, Sheng Z-M, Ely SF, et al (2010) Pulmonary pathologic findings of fatal 2009 pandemic influenza A/H1N1 viral infections. Arch Pathol Lab Med 134:235–243
17. Ruuskanen O, Lahti E, Jennings LC, Murdoch DR (2011) Viral pneumonia. Lancet 377:1264–1275
18. Torres A, Cilloniz C, Niederman MS, et al (2021) Pneumonia. Nat Rev Dis Primers 7:25
19. Chilosi M, Poletti V, Ravaglia C, et al (2021) The pathogenic role of epithelial and endothelial cells in early-phase COVID-19 pneumonia: victims and partners in crime. Mod Pathol 34:1444–1455
20. Gattinoni L, Gattarello S, Steinberg I, et al (2021) COVID-19 pneumonia: pathophysiology and management. Eur Respir Rev 30.: https://doi.org/10.1183/16000617.0138-2021
21. Ceelen W (1913) Über Karnifikation in tuberkulösen Lungen. Virchows Arch Pathol Anat Physiol Klin Med 214:99–132
22. Breining H (1971) [Fatty degeneration of alveolar cover cells]. Pneumonologie 146:64–78

23. Cinti S, Graciotti L, Giordano A, et al (2020) COVID-19 and fat embolism: a hypothesis to explain the severe clinical outcome in people with obesity. Int J Obes 44:1800–1802
24. Nardacci R, Colavita F, Castilletti C, et al (2021) Evidences for lipid involvement in SARS-CoV-2 cytopathogenesis. Cell Death Dis 12:263
25. Grootemaat AE, van der Niet S, Scholl ER, et al (2022) Lipid and Nucleocapsid N-Protein Accumulation in COVID-19 Patient Lung and Infected Cells. Microbiol Spectr 10:e0127121
26. Angermüller S, Fahimi HD (1982) Imidazole-buffered osmium tetroxide: an excellent stain for visualization of lipids in transmission electron microscopy. Histochem J 14:823–835
27. Marshall BE, Hanson CW, Frasch F, Marshall C (1994) Role of hypoxic pulmonary vasoconstriction in pulmonary gas exchange and blood flow distribution. 2. Pathophysiology. Intensive Care Med 20:379–389
28. Schmidt R, Meier U, Yabut-Perez M, et al (2001) Alteration of fatty acid profiles in different pulmonary surfactant phospholipids in acute respiratory distress syndrome and severe pneumonia. Am J Respir Crit Care Med 163:95–100
29. Zheng Y, Ning P, Luo Q, et al (2019) Inflammatory responses relate to distinct bronchoalveolar lavage lipidome in community-acquired pneumonia patients: a pilot study. Respir Res 20:82
30. Ecker J, Liebisch G, Englmaier M, et al (2010) Induction of fatty acid synthesis is a key requirement for phagocytic differentiation of human monocytes. Proc Natl Acad Sci U S A 107:7817–7822
31. Castoldi A, Monteiro LB, van Teijlingen Bakker N, et al (2020) Triacylglycerol synthesis enhances macrophage inflammatory function. Nat Commun 11:4107
32. Jakab GJ (1982) Immune impairment of alveolar macrophage phagocytosis during influenza virus pneumonia. Am Rev Respir Dis 126:778–782
33. Zheng DJ, Abou Taka M, Heit B (2021) Role of Apoptotic Cell Clearance in Pneumonia and Inflammatory Lung Disease. Pathogens 10.: https://doi.org/10.3390/pathogens10020134

**Figures**

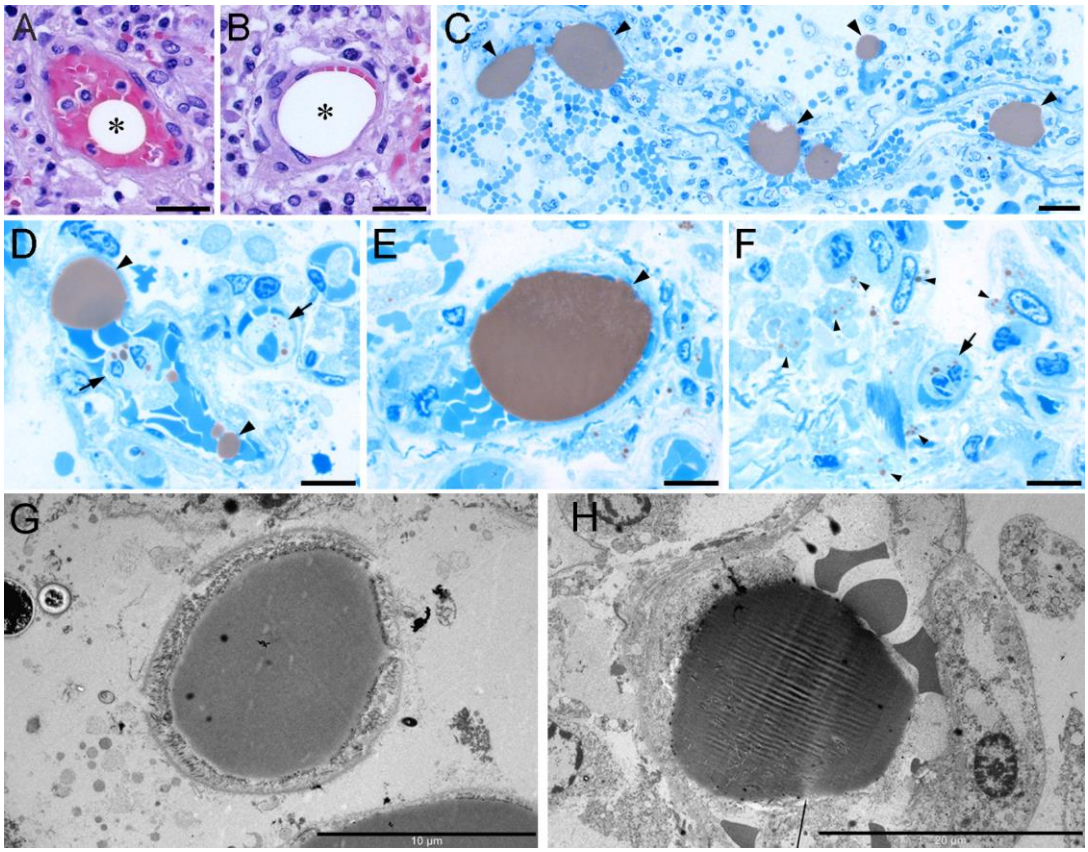


**Figure 1** Lipid droplets in COVID-19–associated pneumonia lung. A. Paraffin section, hematoxylin and eosin staining. A small vessel contains a round cavity (asterisk) surrounded by erythrocytes. Scale bar, 25 µm. B. Paraffin section, hematoxylin and eosin staining. Erythrocytes in a small vessel are deformed and pushed to the vessel wall (asterisk). Scale bar, 25 µm. C. $OsO_4$-contrasted lipid droplets inside blood vessels in the lung. Scale bar, 100 µm. D. $OsO_4$-contrasted lipid droplets are present in the blood vessel (arrows) and in the cells near the vessel (arrowheads). Scale bar, 10 µm. E. $OsO_4$-contrasted lipid droplet fills the blood vessel (arrow), with erythrocytes pushed to the vessel wall. Cells and cell remnants in the vicinity of the vessel contain smaller lipid droplets (arrowheads). Scale bar, 10 µm. F. $OsO_4$-contrasted small lipid droplets in the cytoplasm of the lung-infiltrating neutrophil (large arrowhead) and in other intact and destroyed cells (small arrowheads). Scale bar, 10 µm. G. $OsO_4$-contrasted lipid droplets are homogeneous in ultrathin sections. EM, Scale bar, 10 µm. H. A homogeneous $OsO_4$-contrasted lipid droplet in the blood vessel with erythrocytes; the erythrocytes are pushed to the vessel wall. EM, Scale bar, 20 µm

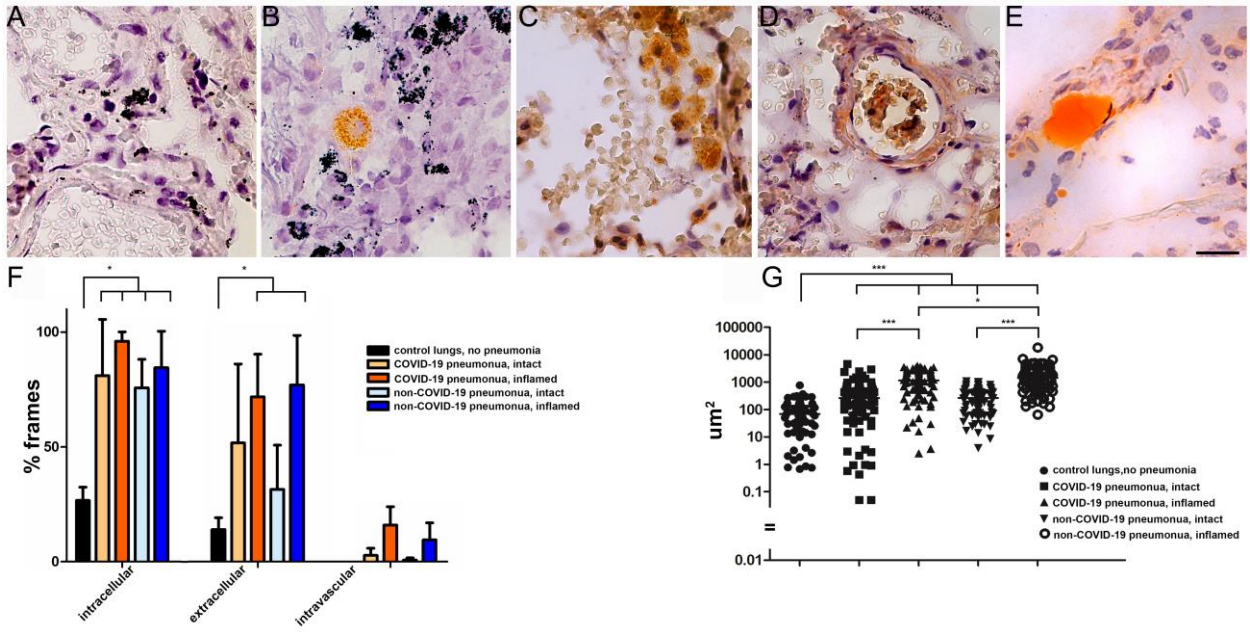


**Figure 2** Lipid distribution in non-pneumonia lung tissue and pneumonias of various etiologies. A. Representative non-pneumonia lung tissue staining with Sudan III: no lipid-rich structures are typically present inside blood vessels, in the vessel walls, or in the alveolar intercepts. Scale bar, 25 µm. B. Representative non-pneumonia lung tissue staining with Sudan III: single cells with lipid-rich cytoplasm in the interalveolar wall present the most common type of Sudan III-positive events in non-pneumonia lung tissue. An example of intracellular lipid deposition is shown. Scale bar, 25 µm. C. Representative pneumonia lung tissue staining with Sudan III (COVID-19–associated pneumonia, inflamed area of the lung): grouped cells with lipid-rich cytoplasm are present in the alveolar intercept and in the vicinity of blood vessels. An example of intracellular lipid deposition is shown. Scale bar, 25 µm. D. Representative pneumonia lung tissue staining with Sudan III (COVID-19-associated pneumonia, inflamed area of the lung): the blood vessel wall contains lipid-rich structures among the elastic fibers. An example of extracellular lipid deposition is shown. Scale bar, 25 µm. E. Representative pneumonia lung tissue staining with Sudan III (COVID-19–associated pneumonia, inflamed area of the lung): blood vessel filled with a lipid droplet. An example of intravascular lipid deposition is shown. Scale bar, 25 µm. F. The occurrence rate of intacellular / extracellular / extravascular lipid deposition in non-pneumonia lung tissue (*n*=3 specimens), COVID-19–associated pneumonia (*n*=4 specimens), and non-COVID-19–associated pneumonia (*n*=4 specimens). Analysis performed on 100 consecutive frames per specimen, occurrence rate determined as percentage of frames containing either type of lipid deposition. Inflamed area of the lung (determined macroscopically) was analyzed along with the intact area of the lung (determined macroscopically and obtained from the upper lobe of the same lung) for each pneumonia case. * statistically significant differences ($p<0.05$, Mann-Whitney test). G. The total area of lipid deposition per frame ($\mu m^2$) in non-pneumonia lung tissue (*n*=3 specimens), COVID-19–associated pneumonia (*n*=4 specimens), and non-COVID-19–associated pneumonia (*n*=4 specimens). The inflamed area of the lung was analyzed along with the intact area of the same lung for each pneumonia case. The total area of lipid deposition was assessed on 20 random frames per specimen; the data from specimens were pooled in their respective groups for further analysis. *, statistically significant differences ($p<0.05$, Mann-Whitney test); ***, statistically significant differences ($p<0.001$, Mann-Whitney test)

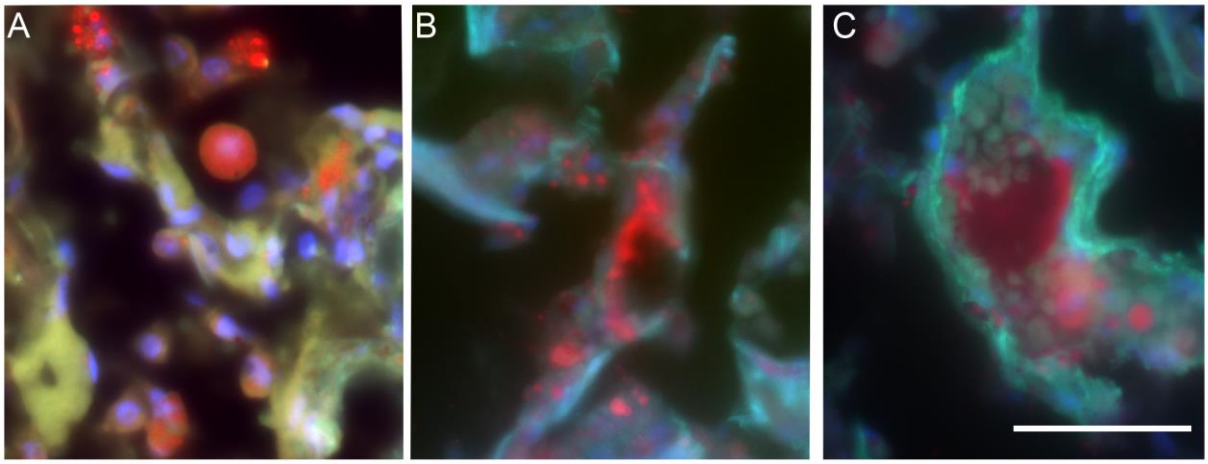


**Figure 3** Representative triple fluorescence staining of pneumonia lung tissue with Oil Red O (red)/anti-CD31 (green)/DAPI (blue). To visualize the Oil Red O staining, anti-CD31-FITC, and DAPI staining, the standard Ex.630 nm/Em.670 nm, Ex.488 nm/Em.520 nm, and Ex.405 nm/Em.430 nm filter cubes were used, respectively. Non-COVID-19–associated pneumonia, inflamed area of the lung. Objective x40/Oil. Scale bar, 50 μm. A. Grouped cells with lipid-rich cytoplasm. An example of intracellular lipid deposition is shown. B. Lipid-rich structures in the blood vessel wall. An example of extracellular lipid deposition is shown. Objective x40/Oil. Scale bar, 50 μm. C. blood vessel filled with erythrocytes and a lipid droplet. An example of intravascular lipid deposition is shown. Objective x40/Oil. Scale bar, 50 μm

**Supplementary Information**

**Supplementary Figures**

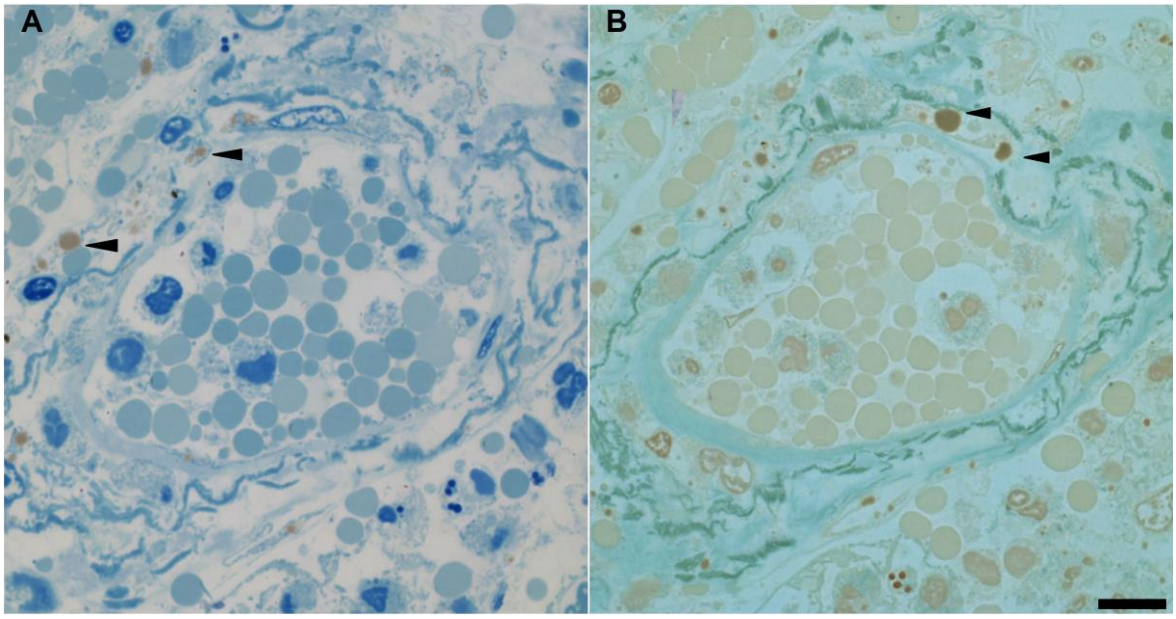


**Supplementary Figure S1** Comparison of methylene blue/azure II and Twort's staining of lipid-rich structures in COVID-19–associated pneumonia. A. The lipid depositions are clearly visible in lung tissue methylene blue/azure II specimens; the lipid-rich structures in this case have brown color (arrowheads) that distinguishes them from other cellular and extracellular structures, which have blue color. B. The color differentiation between lipid droplets and erythrocytes is not so obvious with Twort's staining: the lipid droplets in this case have dark brown color (arrowheads), while the erythrocytes have pale brown color. Scale bar, 10 μm.

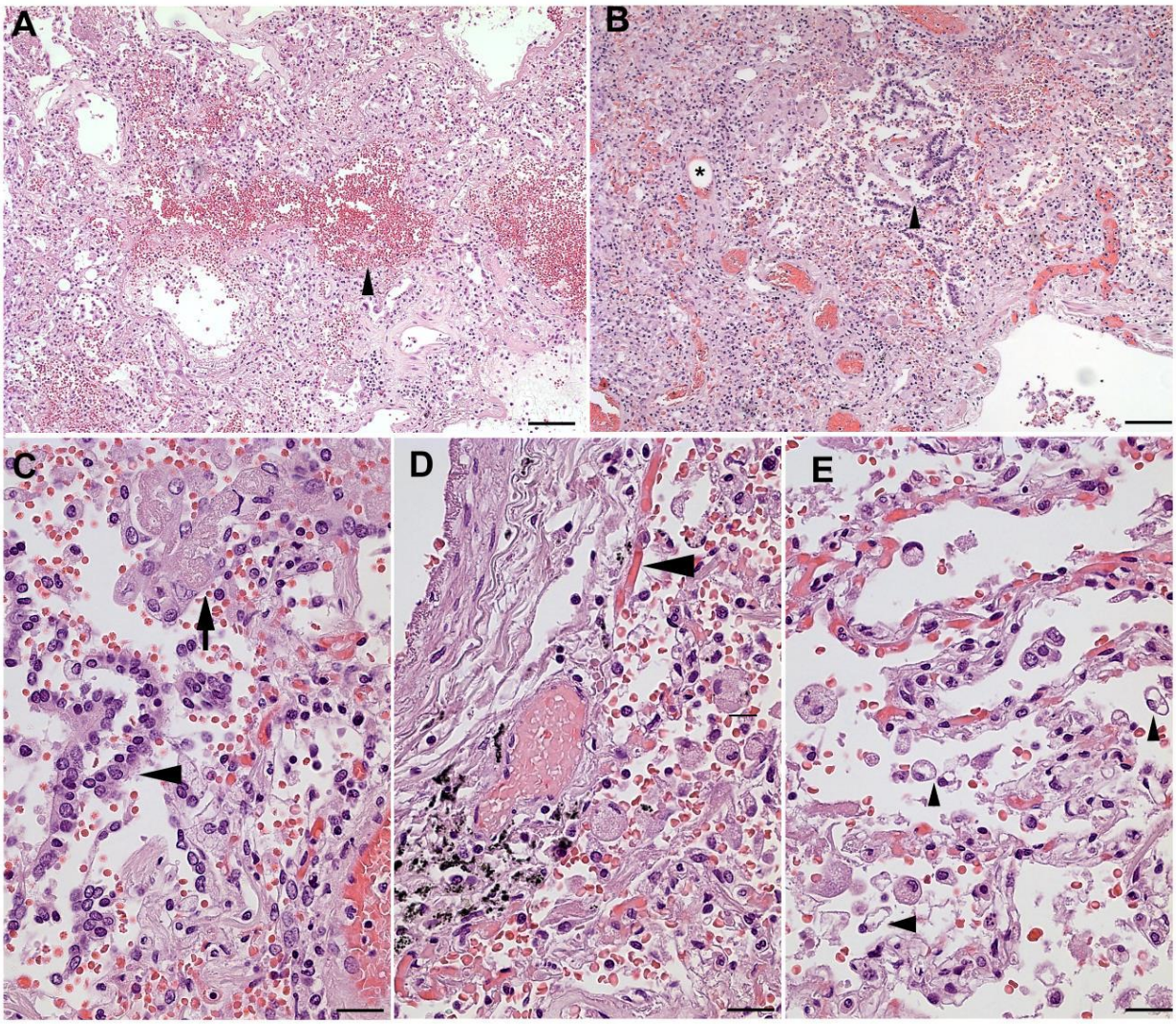


**Supplementary Figure S2** H&E paraffin sections of COVID-19–associated pneumonias, characteristic changes of lung tissue morphology. A. Exudative stage of diffuse alveolar damage, loss of lung morphology; fields of extravascular erythrocytes within lung tissue (arrowhead). Scale bar, 100 µm. B. Proliferative stage of diffuse alveolar damage, loss of lung morphology; alveolar remnants contain desquamed epithelial cells (arrowhead). The blood vessels are filled with erythrocytes; surrounded by erythrocytes is the cavity that presumably contained a lipid droplet (asterisk). Scale bar, 100 µm. C. Alveolar remnants with giant cells (arrow) and desquamed epithelium (arrowhead). Scale bar, 25 µm. D. Blood vessels filled with erythrocytes. Characteristic erythrocyte sludges in capillaries (arrowhead). Scale bar, 25 µm. E. Apart from erythrocyte sludges in the capillaries, cells with foamed cytoplasm or empty cavities in the cytoplasm are present near the vessels (arrowheads). Scale bar, 25 µm

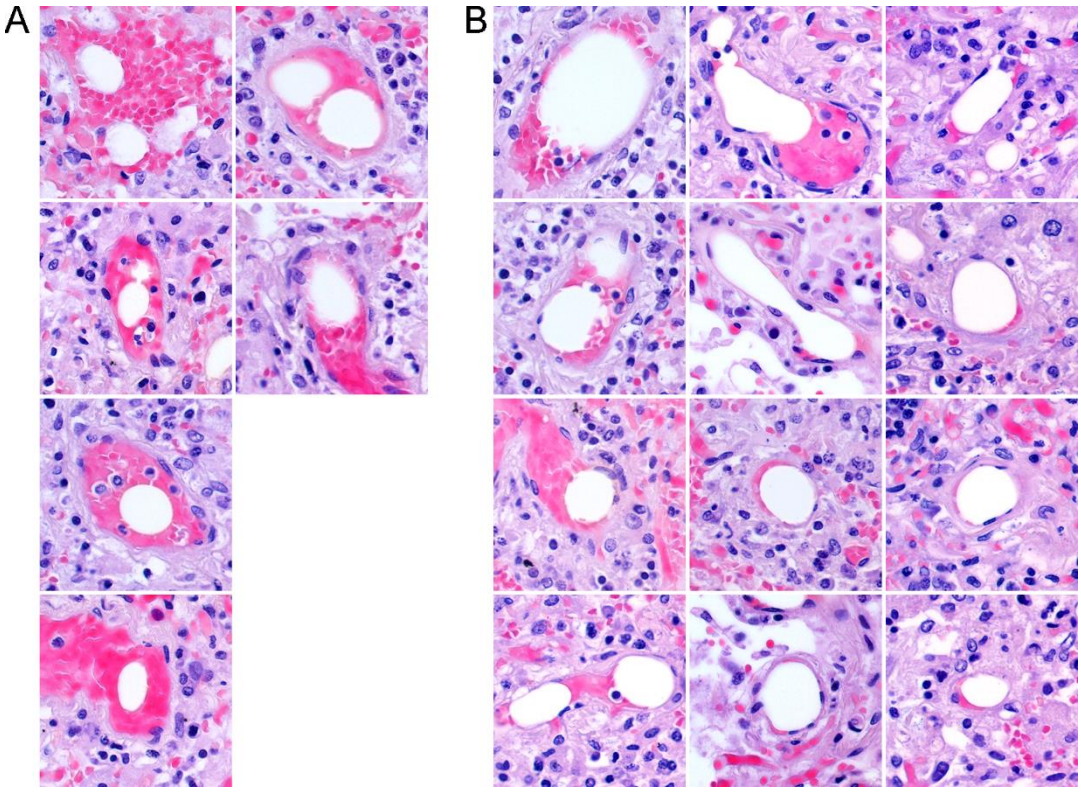


**Supplementary Figure S3** The image gallery obtained upon the examination of a single random H&E specimen of COVID-19–associated pneumonia. The majority of the blood vessels in pneumonia lungs are filled with erythrocytes. A. A large number of vessels contain cavities, completely surrounded by erythrocytes, which presumably contained lipid-rich structures lost upon specimen dehydration. B. Other vessels contain deformed erythrocytes pushed to the side of the vessel. The sizes of the cavities are close to the sizes of small vessels.

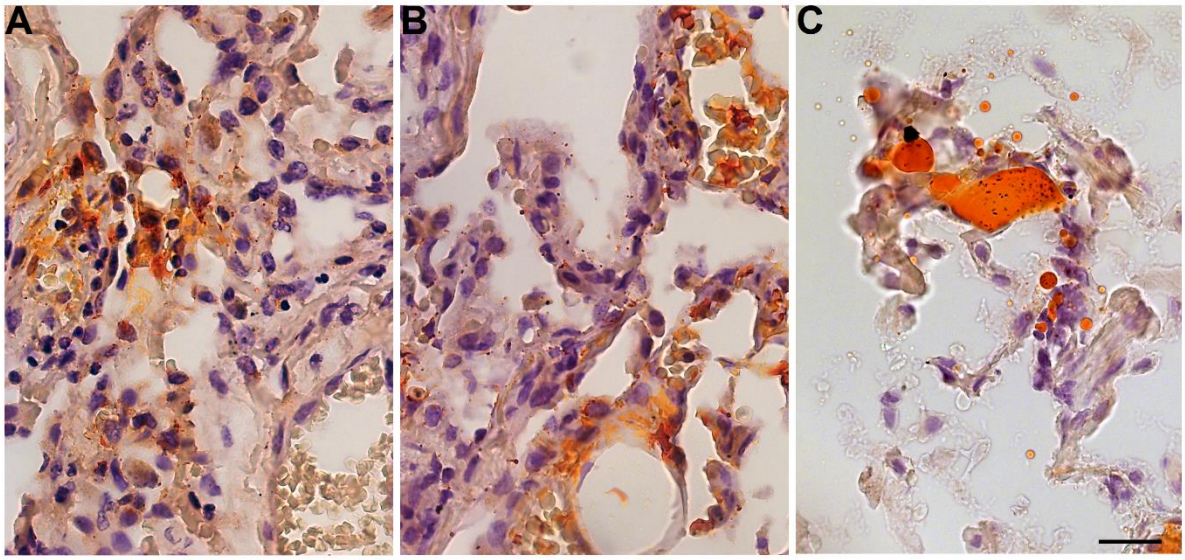


**Supplementary Figure S4** The lipid distribution in non-COVID-19–associated pneumonia. A. Representative pneumonia lung tissue staining with Sudan III (non-COVID-19–associated pneumonia, inflamed area of the lung): grouped cells with lipid-rich cytoplasm are present in the alveolar intercept and in the vicinity of blood vessels. An example of intracellular lipid deposition is shown. Scale bar, 25 µm. B. Representative pneumonia lung tissue staining with Sudan III (non-COVID-19-associated pneumonia, inflamed area of the lung): the blood vessel wall contains lipid-rich structures among the elastic fibers. An example of extracellular lipid deposition is shown. Scale bar, 25 µm. C. Representative pneumonia lung tissue staining with Sudan III (non-COVID-19–associated pneumonia, inflamed area of the lung): blood vessel filled with a lipid droplet. An example of intravascular lipid deposition is shown. Scale bar, 25 µm.

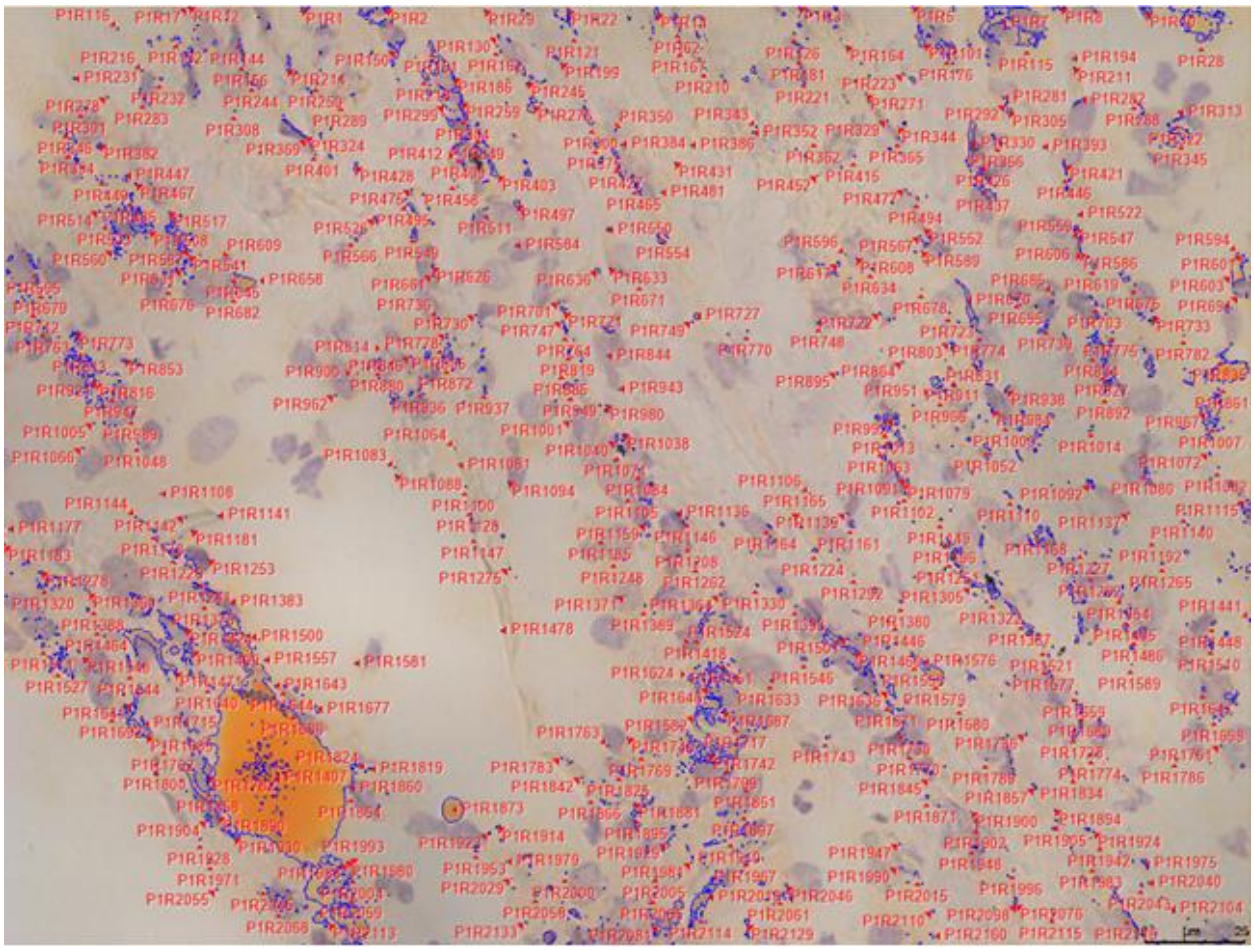

**Supplementary Figure S5** Example of the morphometric analysis of Sudan III-stained lung cryosections. For each image, Sudan III–positive droplets were included in an ImagePro mask containing pixels by color. The mask was created semi-automatically based on the operator-chosen pixel color, and manually adjusted to include all Sudan III–positive structures into the regions of interest (ROIs). The total area of the mask was calculated in $\mu m^2$. Scale bar, 25 µm.

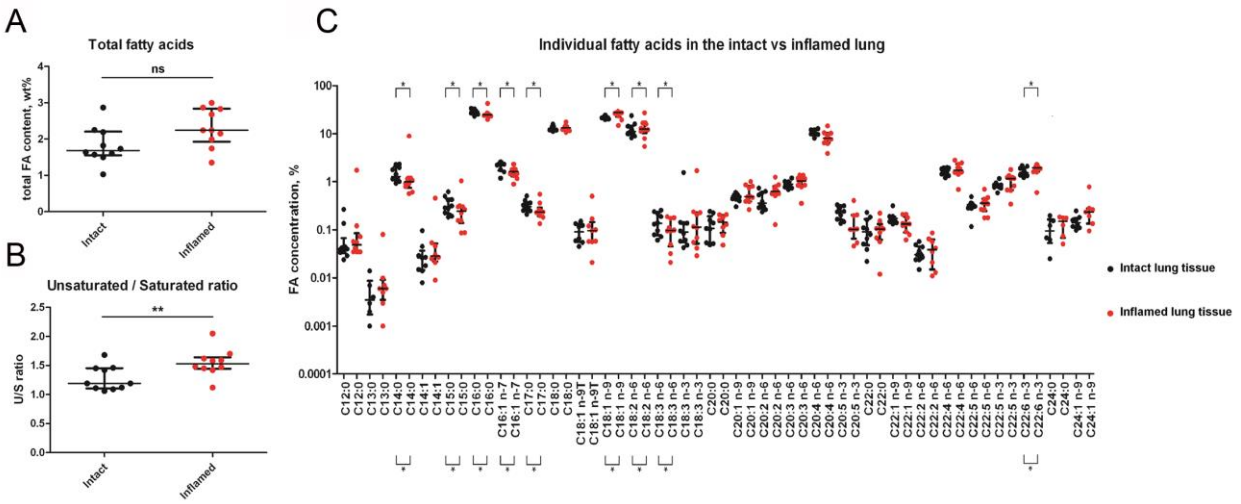


**Supplementary Figure S6** The lipid content of the inflamed vs. intact sections of lung tissue with pneumonia assessed with chromato-mass spectrometry. A. Total fatty acid (FA) content in inflamed pneumonia and intact pneumonia lung specimens. The differences are statistically insignificant. B. The ratio of unsaturated to saturated fatty acids per specimen. The difference is statistically significant (Wilcoxon test, $p<0.01$). C. The concentrations of individual fatty acids. The difference is statistically significant for 9 fatty acids (Wilcoxon test, $p<0.05$). The saturated fatty acids C14:0 (tetradecanoic, myristic), C15:0 (pentadecanoic), C16:0 (hexadecanoic, palmitic), and C17:0 (heptadecanoic, margaric), and the unsaturated fatty acids C16:1 n-7 (palmitoleic) and C18:3 n-6 (γ-linolenic) were significantly decreased in the inflamed area of the lung compared to the macroscopically intact area, whereas the unsaturated fatty acids C18:1 n-9 (oleic), C18:2 n-6 (α-linoleic), and C22:6 n-3 (docosahexaeoic) were significantly elevated in the inflamed area of the lung compared to the macroscopically intact area.

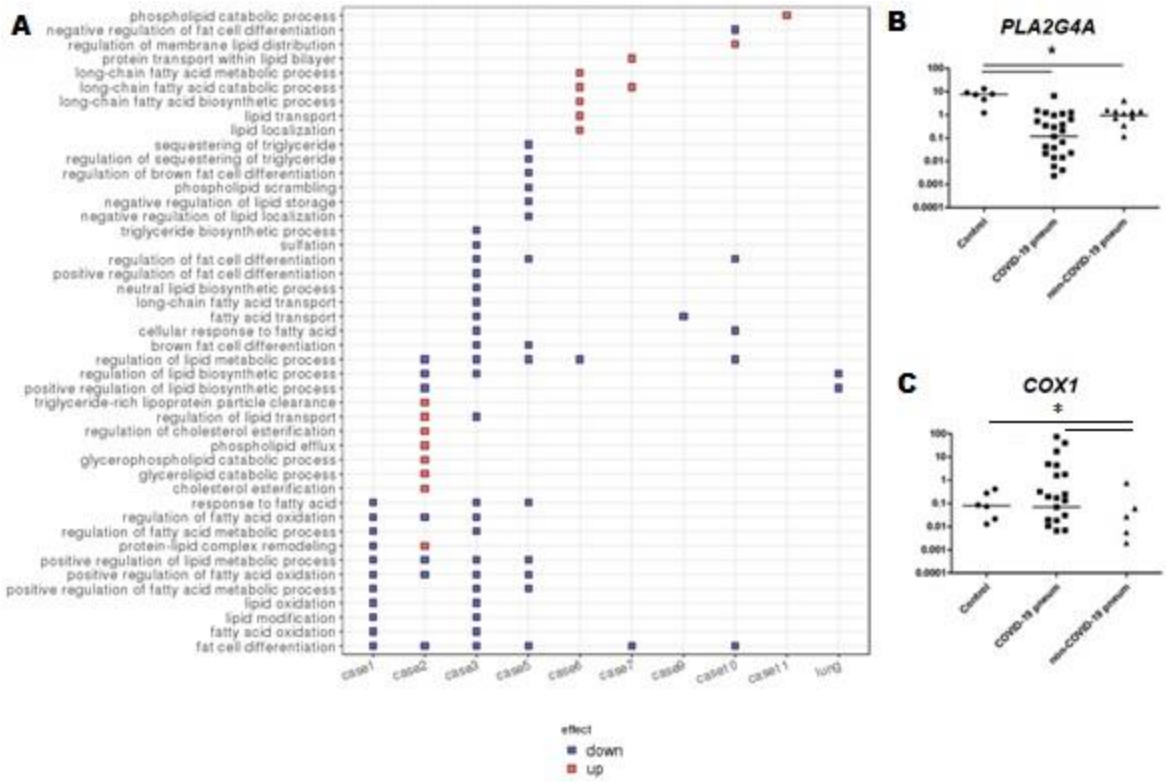


**Supplementary Figure S7.** GO and qPCR analysis. A. The bulk RNA-seq dataset analysis included 9 independent pneumonia cases (“case1”; “case2”; “case3”; “case5”; “case6”; “case7”; “case9”; “case10”; “case11”) and the data on the cumulative dataset (“lung”). The alterations were found in a number of gene clusters, including those specified by GO terms “regulation of lipid biosynthetic process” and “positive regulation of lipid biosynthetic process” (for the cumulative dataset), “fat cell differentiation” (for 6 of 9 cases), and “regulation of lipid metabolic process” (for 5 of 9 cases). The overall trend for gene downregulation is observed despite the variability between cases. B. Relative normalized gene expression data, *PLA2G4A*, qPCR. *, statistically significant differences ($p<0.05$, Mann-Whitney test). C. Relative normalized gene expression data, *COX1*, qPCR. *, statistically significant differences ($p<0.05$, Mann-Whitney test).

**Supplementary Tables**

**Supplementary Table S1.** Description of the autopsies included in the study.

| Autopsy | Sex | Age | Pneumonia | COVID-19 in-hospital qPCR | COVID-19 post-mortem qPCR | BMI |
|---|---|---|---|---|---|---|
| **1 COVID-19** | F | 82 | + | NA | + | BMI<30 |
| **2 COVID-19** | M | 79 | + | + | + | NA |
| **3 COVID-19** | F | 68 | + | NA | + | BMI≥30 |
| **4 COVID-19** | F | 61 | + | + | + | BMI≥30 |
| **5 COVID-19** | M | 79 | + | + | + | NA |
| **6 COVID-19** | M | 62 | + | + | + | NA |
| **7 COVID-19** | M | 73 | + | + | + | BMI≥30 |
| **8 COVID-19** | M | 79 | + | + | + | BMI≥30 |
| **9 COVID-19** | F | 78 | + | - | + | BMI<30 |
| **10 COVID-19** | M | 73 | + | - | + | BMI<30 |
| **11 COVID-19** | M | 89 | + | + | + | BMI≥30 |
| **12 COVID-19** | M | 74 | + | + | + | BMI<30 |
| **13 COVID-19** | F | 84 | + | + | + | BMI<30 |
| **14 COVID-19** | F | 70 | + | + | NA | BMI<30 |
| **15 COVID-19** | M | 84 | + | + | NA | BMI<30 |
| **16 COVID-19** | F | 67 | + | + | NA | 24,7 |
| **17 COVID-19** | M | 62 | + | - | + | BMI<30 |
| **18 COVID-19** | M | 61 | + | - | + | 15,6 |
| **19 COVID-19** | F | 87 | + | NA | + | BMI<30 |
| **20 COVID-19** | M | 71 | + | - | + | BMI<30 |
| **21 COVID-19** | M | 71 | + | - | + | NA |
| **22 COVID-19** | F | 63 | + | - | + | 31,5 |

| | | | | | | |
|---|---|---|---|---|---|---|
| **23 COVID-19** | F | 80 | + | NA | + | 18.5 |
| | | | | | | |
| **1 non-COVID-19** | M | 54 | + | - | - | 24,8 |
| **2 non-COVID-19** | M | 67 | + | - | - | BMI<30 |
| **3 non-COVID-19** | M | 40 | + | - | - | 32,8 |
| **4 non-COVID-19** | F | 76 | + | - | - | BMI<30 |
| **5 non-COVID-19** | F | 47 | + | - | - | 28 |
| **6 non-COVID-19** | M | 61 | + | - | - | BMI<30 |
| **7 non-COVID-19** | M | 89 | + | - | - | BMI<30 |
| **8 non-COVID-19** | F | 89 | + | - | - | 19,5 |
| **9 non-COVID-19** | F | 73 | + | - | - | 28 |
| **10 non-COVID-19** | M | 89 | + | - | - | 22 |
| **11 non-COVID-19** | M | 75 | + | - | - | 23,1 |
| **12 non-COVID-19** | M | 82 | + | - | - | BMI<30 |
| **13 non-COVID-19** | M | 81 | + | - | - | 24,6 |
| **14 non-COVID-19** | F | 59 | + | - | - | 18.5 |
| **15 non-COVID-19** | F | 80 | + | NA | - | 33,7 |
| **16 non-COVID-19** | F | 62 | + | NA | - | 37,2 |
| **17 non-COVID-19** | F | 61 | + | - | - | 28,4 |
| **18 non-COVID-19** | M | 68 | + | NA | - | 25,3 |
| | | | | | | |
| **1 Ctrl** | F | 95 | - | NA | - | BMI<30 |
| **2 Ctrl** | M | 90 | - | NA | - | BMI<30 |
| **3 Ctrl** | F | 74 | - | NA | - | BMI<30 |
| **4 Ctrl** | F | 67 | - | NA | - | BMI<30 |
| **5 Ctrl** | M | 57 | - | NA | - | BMI<30 |
| **6 Ctrl** | F | 64 | - | NA | - | BMI<30 |

| | | | | | | |
|---|---|---|---|---|---|---|
| **7 Ctrl** | F | 84 | - | NA | - | BMI<30 |
| **8 Ctrl** | M | 84 | - | NA | - | 32,4 |
| **9 Ctrl** | F | 73 | - | NA | - | 20,2 |
| **10 Ctrl** | M | 69 | - | NA | - | 32,1 |

*BMI, body mass index. NA, data not available.

**Supplementary Table S2.** qPCR primers and probes for SARS-CoV-2 detection in lung tissue.

| Name | Sequence | Label |
|---|---|---|
| ***N2*-forward** | TTACAAACATTGGCCGCAAA | - |
| ***N2*-reverse** | GCGCGACATTCCGAAGAA | - |
| ***N2*-probe** | ACAATTTGCCCCCAGCGCTTCAG | 5’-FAM 3’-BHQ1 |
| ***N3*-forward** | GGGAGCCTTGAATACACCAAAA | - |
| ***N3*-reverse** | TGTAGCACGATTGCAGCATTG | - |
| ***N3*-probe** | ATCACATTGGCACCCGCAATCCTG | 5’-VIC 3’-BHQ2 |
| ***UBC*-forward** | TTGGGTCGCAGTTCTTGTTTG | - |
| ***UBC*-reverse** | TGCCTTGACATTCTCGATGGT | - |
| ***UBC*-probe** | TCGCTGTGATCGTCACTTGACAATG | 5’-ROX 3’-BHQ2 |

*The *N2* and *N3* sequences used were recommended for SARS-CoV-2 detection by the Division of Viral Diseases, National Center for Immunization and Respiratory Diseases, Centers for Disease Control and Prevention, Atlanta, GA, USA. *UBC* was added as a reference gene. All oligonucleotides were synthesized with DNK-Sintez (Russia) and put into a triplex one-step qPCR reaction. Sequences are presented in 5′–3′direction. FAM, fluorescein; VIC, 2′-chloro-7′phenyl-1,4-dichloro-6-carboxy-fluorescein; ROX, carboxyrhodamine; BHQ1/2, Black Hole Quencher 1/2.

**Supplementary Table S3.** qPCR primers and probes for the detection of genes of interest in lung tissue.

| Name | Sequence | Label |
|---|---|---|
| ***COX1*-forward** | TTCTTGCTGTTCCTGCTCCT | - |
| ***COX1*-reverse** | TGACAAACTCCCAGAACCAG | - |
| ***COX1*-probe** | CCTTGACCGCTACCAGTGTGA | 5’-FAM 3’-BHQ1 |
| ***COX2*-forward** | GATGATTGCCCGACTCCCTT | - |
| ***COX2*-reverse** | CTAGCCAGAGTTTCACCGTAA | - |
| ***COX2*-probe** | CCCAGCACTTCACGCATCAGTT | 5’-VIC 3’-BHQ2 |
| ***UBC*-forward** | TTGGGTCGCAGTTCTTGTTTG | - |
| ***UBC*-reverse** | TGCCTTGACATTCTCGATGGT | - |
| ***UBC*-probe** | TCGCTGTGATCGTCACTTGACAATG | 5’-ROX 3’-BHQ2 |
| ***LPL*-forward** | GTGCCAGAACTTCGACCCTT | - |
| ***LPL*-reverse** | TTTTCGGAGCCAGAGTTCCC | - |
| ***LPL*-probe** | GATGATCGTGCCTATAAATAGTAG | 5’-FAM 3’-BHQ1 |
| ***PLA2G4A*-forward** | ATCACACGAACCCAAAGGCA | - |
| ***PLA2G4A* -reverse** | AGCCCAGCATGAAGTTGTGT | - |
| ***PLA2G4A* -probe** | GGTGAGTGATTCAGCTTTATTCAATACC | 5’-VIC 3’-BHQ2 |
| ***PLA2G2A*-forward** | GGAGTGCAGAACAAACAAGAC | - |
| ***PLA2G2A* -reverse** | GCAGCCGTAGAAGCCATAAC | - |
| ***PLA2G2A* -probe** | ACCATGAAGACCCTCCTACTGTTGG | 5’-ROX 3’-BHQ2 |

* All oligonucleotides were synthesized by DNK-Sintez (Russia) and used in two triplex qPCR reactions (*COX1+COX2+UBC* and *LPL+PLA2G4A+PLA2G2A*) to analyze cDNA obtained from lung tissue. Sequences are presented in 5′–3′ direction. FAM, fluorescein; VIC, 2′-chloro-7′phenyl-1,4-dichloro-6-carboxy-fluorescein; ROX, carboxyrhodamine; BHQ1/2, Black Hole Quencher 1/2.

**Supplementary Table S4.** Lipid droplet distribution in lung tissue; morphologic and morphometric analysis.

| Specimen | Number of frames with: | | | Total area of lipid droplets, μm$^2$ | |
|---|---|---|---|---|---|
| | Intracellular lipid droplets / per 100 frames | Extracellular lipid droplets / per 100 frames | Intra-vessel lipid droplets / per 100 frames | Median / per 20 frames | IQR* / per 20 frames |
| **Non-pneumonia lung 1** | 30 | 11 | 0 | 39.71 | 10.26-89.42 |
| **Non-pneumonia lung 2** | 20 | 11 | 0 | 76.57 | 27.53-131.33 |
| **Non-pneumonia lung 3** | 30 | 20 | 0 | 73.87 | 31.45-168.94 |
| **Non-COVID-19 pneumonia, intact lung 1** | 65 | 30 | 1 | 327.60 | 236.26-428.28 |
| **Non-COVID-19 pneumonia, intact lung 2** | 93 | 12 | 0 | 75.95 | 51.76-270.78 |
| **Non-COVID-19 pneumonia, intact lung 3** | 76 | 58 | 0 | 404.75 | 199.51-732.86 |
| **Non-COVID-19 pneumonia, intact lung 4** | 69 | 26 | 2 | 162.87 | 74.32-415.88 |
| **Non-COVID-19 pneumonia, inflamed lung 1** | 96 | 89 | 0 | 1,178.58 | 706.10-1672.91 |
| **Non-COVID-19 pneumonia, inflamed lung 2** | 100 | 100 | 18 | 2,930.49 | 2081.97-4,549.38 |
| **Non-COVID-19 pneumonia, inflamed lung 3** | 74 | 67 | 11 | 1,759.32 | 642.48-2,347.01 |
| **Non-COVID-19 pneumonia, inflamed lung 4** | 68 | 52 | 9 | 506.99 | 313.01-1,559.79 |
| **COVID-19 pneumonia, intact lung 1** | 45 | 19 | 1 | 47.97 | 2.74-194.60 |
| **COVID-19 pneumonia, intact lung 2** | 90 | 47 | 7 | 348.75 | 163.46-704.57 |
| **COVID-19 pneumonia, intact lung 3** | 89 | 41 | 3 | 313.58 | 123.13-773.69 |
| **COVID-19 pneumonia, intact lung 4** | 100 | 100 | 0 | 443.24 | 261.63-660.08 |

| | | | | | |
|---|---|---|---|---|---|
| **COVID-19 pneumonia, inflamed lung 1** | 99 | 59 | 5 | 546.49 | 107.84-1,082.08 |
| **COVID-19 pneumonia, inflamed lung 2** | 93 | 72 | 18 | 1,236.84 | 619.31-2,516.79 |
| **COVID-19 pneumonia, inflamed lung 3** | 92 | 58 | 17 | 1,056.92 | 235.39-1,428.66 |
| **COVID-19 pneumonia, inflamed lung 4** | 100 | 98 | 24 | 2,189.44 | 1415.08 – 2,738.02 |

* IRQ, interquartile range

**Supplementary Table S5**. Single-cell RNAseq analysis.

| Cell Type | Tissue | Gene ID | Up/Down |
|---|---|---|---|
| **Alveolartype II cells** | Lung | *MSMO1* | Upregulated |
| **Alveolartype II cells** | Lung | *SCD* | Upregulated |
| **Alveolartype II cells** | Lung | *FDFT1* | Upregulated |
| **Alveolartype II cells** | Lung | *HMGCS1* | Upregulated |
| **Alveolartype II cells** | Lung | *FASN* | Upregulated |
| **Fibroblasts** | Lung | *FGF2* | Downregulated |
| **Fibroblasts** | Lung | *RARRES2* | Downregulated |
| **Fibroblasts** | Lung | *DKK3* | Downregulated |
| **Fibroblasts** | Lung | *PDGFRA* | Downregulated |
| **Fibroblasts** | Lung | *FGFR4* | Downregulated |
| **Endothelialcells** | Lung | *FLT1* | Upregulated |
| **Endothelialcells** | Lung | *RELN* | Upregulated |
| **Endothelialcells** | Lung | *PIK3R3* | Downregulated |
| **Endothelialcells** | Lung | *PDGFB* | Downregulated |
| **Endothelialcells** | Lung | *FGF2* | Downregulated |
| **Macrophages** | Lung | *PSAP* | Upregulated |
| **Macrophages** | Lung | *SPP1* | Upregulated |
| **Macrophages** | Lung | *GLUL* | Upregulated |
| **Macrophages** | Lung | *FABP4* | Downregulated |
| **Macrophages** | Lung | *RBP4* | Downregulated |
| **Macrophages** | Lung | *RETN* | Downregulated |
| **Macrophages** | Lung | *INHBA* | Downregulated |
| **Macrophages** | Lung | *PPARG* | Downregulated |
| **Macrophages** | Lung | *FFAR4* | Downregulated |

| | | | |
|---|---|---|---|
| **Macrophages** | Lung | *LPL* | Downregulated |
| **Macrophages** | Lung | *FABP3* | Downregulated |
| **Macrophages** | Lung | *NMB* | Downregulated |
| **Macrophages** | Lung | *ADTRP* | Downregulated |
| **Macrophages** | Lung | *AKR1C2* | Downregulated |
| **Macrophages** | Lung | *SCD* | Downregulated |
| **Macrophages** | Lung | *AKR1C3* | Downregulated |
| **Monocytes** | Lung | *ABHD5* | Upregulated |
| **Monocytes** | Lung | *G0S2* | Upregulated |
| **Monocytes** | Lung | *HCAR2* | Upregulated |
| **Monocytes** | Lung | *ANXA2* | Downregulated |
| **Monocytes** | Lung | *THBS1* | Downregulated |
| **T cells** | Lung | *IFNG* | Upregulated |
| **T cells** | Lung | *FYN* | Upregulated |
| **T cells** | Lung | *CCL5* | Upregulated |
| **T cells** | Lung | *LIPA* | Downregulated |
| **T cells** | Lung | *FUCA1* | Downregulated |
| **T cells** | Lung | *APOE* | Downregulated |
| **T cells** | Lung | *APOC1* | Downregulated |
| **T cells** | Lung | *APOC2* | Downregulated |
| **T cells** | Lung | *PLTP* | Downregulated |
| **T cells** | Lung | *FABP3* | Downregulated |
| **T cells** | Lung | *FABP4* | Downregulated |
| **T cells** | Lung | *SCD* | Downregulated |

* The tissue type in analysis was restricted to "Lung" and the cell types in analysis were restricted to the most prominent resident/infiltrating cell populations. The genes showing controversial results in different datasets were excluded. In the lung tissue, the downregulated genes in lung tissue are mostly assigned to fibroblasts (5

downregulated genes), macrophages (13 downregulated genes, 3 upregulated genes), and T cells (9 downregulated genes, 3 upregulated genes).